

DRAFT

CMS Paper

The content of this note is intended for CMS internal use and distribution only

2015/01/23

Head Id: 274664

Archive Id: 274773P

Archive Date: 2015/01/22

Archive Tag: trunk

Measurements of the $Y(1S)$, $Y(2S)$, and $Y(3S)$ differential cross sections in pp collisions at $\sqrt{s} = 7$ TeV

The CMS Collaboration

Abstract

Differential cross sections as a function of transverse momentum p_T are presented for the production of $Y(nS)$ ($n = 1, 2, 3$) states decaying into a pair of muons. Data corresponding to an integrated luminosity of 4.9 fb^{-1} in pp collisions at $\sqrt{s} = 7$ TeV were collected with the CMS detector at the LHC. The analysis selects events with dimuon rapidity $|y| < 1.2$ and dimuon transverse momentum in the range $10 < p_T < 100$ GeV. The measurements show a transition from an exponential to a power-law behavior at $p_T \approx 20$ GeV for the three Y states. Above that transition, the $Y(3S)$ spectrum is significantly harder than that of the $Y(1S)$ and $Y(2S)$. The ratios of the $Y(3S)$ and $Y(2S)$ differential cross sections to the $Y(1S)$ cross section show a rise as p_T increases at low p_T , then become flatter at higher p_T .

This box is only visible in draft mode. Please make sure the values below make sense.

PDFAuthor: Benjamin Carlson, James Russ

PDFTitle: Upsilon“(1S”), Upsilon“(2S”), and Upsilon“(3S”) differential cross section measurements in pp collisions at sqrt“(s”) = 7 TeV

PDFSubject: CMS

PDFKeywords: CMS, Upsilon, B-Physics, cross section

Please also verify that the abstract does not use any user defined symbols

1 Introduction

Hadronic production of S-wave $b\bar{b}$ mesons has been extensively studied for many years. At the CERN LHC, the CMS [1, 2], ATLAS [3], and LHCb [4] Collaborations have published results on $Y(nS)$ ($n = 1, 2, 3$) production cross sections times dimuon branching fractions in pp collisions at $\sqrt{s} = 7$ TeV as a function of the Y transverse momentum p_T , rapidity y , and polarization [5]. The CMS and ATLAS p_T and $|y|$ distributions in the central rapidity region $|y| < 2.0$ are similar in shape to those from $p\bar{p}$ production at $\sqrt{s} = 1.96$ TeV, as measured by the D0 [6] and CDF [7] experiments at the Tevatron. Neither the ATLAS nor the CMS results show any statistically significant rapidity dependence of the cross section in the central region. The CMS analyses cover the p_T range up to 50 GeV, while the ATLAS results go to 70 GeV.

In this Letter we present a measurement of the differential production cross sections of the three lowest-mass $Y(nS)$ states in pp collisions at $\sqrt{s} = 7$ TeV up to $p_T = 100$ GeV, reaching higher p_T than previous measurements. We measure the p_T dependence of the $Y(nS)$ differential cross section times the branching fraction to $\mu^+\mu^-$ using the 2011 data set, corresponding to an integrated luminosity of 4.9 fb^{-1} . The measured cross sections include feeddown from higher $b\bar{b}$ excitations.

Measurements of S-wave $b\bar{b}$ mesons provide an important probe of quantum chromodynamics (QCD). There are several models that predict differential cross section shapes at high $Y(nS)$ p_T in pp collisions. A common feature of all the models is that different contributing terms have different p_T variations, some of which are power-law forms. The nonrelativistic QCD (NRQCD) approach [8, 9] uses an effective field theory to factorize the perturbative term and nonperturbative long-distance matrix element (LDME) terms. A good description of early LHC results for $Y(1S)$ production for $p_T < 30$ GeV was achieved using NRQCD with next-to-leading-order (NLO) corrections [10]. However, there are theoretical corrections to perturbative NRQCD that have characteristic power-law behavior at high p_T , and measurements at high p_T can help to clarify the theoretical picture [11, 12]. The NLO NRQCD calculation has recently been extended to treat all three $Y(nS)$ states [13]. The updated calculation includes not only NLO terms but also uses LDMEs computed using only high- p_T data. Color singlet models (CSM) with higher-order p_T -dependent corrections [14] and the k_t -factorization model [15] are consistent with data from the LHC for p_T approaching 50 GeV. A recent analysis of quarkonium polarization and production measurements found that raising p_T thresholds stabilizes the fits in evaluating the LDMEs [16]. At higher p_T different corrections become dominant in these models. New data at high p_T will challenge all the current approaches.

2 CMS detector

The central feature of the CMS apparatus is a superconducting solenoid of 6 m internal diameter having a 3.8 T field. Within the superconducting solenoid volume are a silicon pixel and strip tracker, a lead tungstate crystal electromagnetic calorimeter, and a brass and scintillator hadron calorimeter. Muons are measured in gas-ionization detectors embedded in the steel flux-return yoke outside the solenoid, with detection planes made using three technologies: drift tubes, cathode strip chambers, and resistive-plate chambers. Muons are measured in the pseudorapidity range $|\eta| < 2.4$.

The silicon tracker measures charged particles within the pseudorapidity range $|\eta| < 2.5$. It consists of 1440 silicon pixel and 15148 silicon strip detector modules and provides a typical transverse impact parameter resolution of 25–90 μm . Matching muons to tracks measured in the silicon tracker results in a transverse momentum resolution between 1% and 2.8%, for p_T

values up to 100 GeV [17].

The first level of the CMS trigger system, composed of custom hardware processors, uses information from the calorimeters and muon detectors to select the most interesting events in a fixed time interval of less than 4 μ s. The high-level trigger processor farm further decreases the event rate from around 100 kHz to around 400 Hz, before data storage. A more detailed description of the CMS detector, together with a definition of the coordinate system used and the relevant kinematic variables, can be found in Ref. [18].

3 Differential cross section measurement methodology

Event selection starts with a dimuon trigger involving the silicon tracker and muon systems. The trigger requires at least two muons with dimuon rapidity $|y| < 1.25$, dimuon invariant mass $8.5 < M_{\mu\mu} < 11.5$ GeV, and a dimuon vertex fit with a χ^2 probability $> 0.5\%$. The trigger selects only pairs of muons that bend away from each other in the magnetic field ("seagull selection"). Trigger p_T thresholds varied from 5–9 GeV as the beam conditions changed. Offline selection criteria required $p_T > 10$ GeV, $|y| < 1.2$, and a dimuon vertex fit χ^2 probability $> 1\%$. Standard CMS quality requirements are used to identify muons and muons are restricted to $|\eta(\mu)| < 1.6$. The muon tracks are required to have at least ten hits in the silicon tracker, at least one hit in the silicon pixel detector, and be matched with at least one segment of the muon system. The muon track fit quality must have a χ^2 per degree of freedom of less than 1.8. The distance of the track from the closest primary vertex must be less than 15 cm in the longitudinal direction and 3 cm in the transverse direction. The following kinematic requirements are also imposed to ensure accurate muon detection efficiency evaluation:

$$\begin{aligned} p_T(\mu) &> 3 \text{ GeV for } 1.4 < |\eta(\mu)| < 1.6, \\ p_T(\mu) &> 3.5 \text{ GeV for } 1.2 < |\eta(\mu)| < 1.4, \\ p_T(\mu) &> 4.5 \text{ GeV for } |\eta(\mu)| < 1.2. \end{aligned} \quad (1)$$

The differential cross sections are measured for two rapidity ranges: $|y| \leq 0.6$ and $0.6 < |y| < 1.2$, as well as for the entire range $|y| < 1.2$. In each rapidity range the data are binned in p_T , with bin edges at 2 GeV intervals between 10 and 40 GeV, then wider bins with edges at 43, 46, 50, 55, 60, 70, and 100 GeV.

The $Y(nS)$ differential cross section times dimuon branching fraction, integrated over either of the two $|y|$ ranges and in a given p_T bin of width Δp_T , is

$$\left. \frac{d\sigma(\text{pp} \rightarrow Y(nS))}{dp_T} \right|_{|y|\text{range}} \times \mathcal{B}(Y(nS) \rightarrow \mu^+\mu^-) = \frac{N_{Y(nS)}^{\text{fit}}(p_T)}{L \cdot \Delta p_T \cdot \epsilon_{\mu\mu}(p_T) \cdot \mathcal{A}(p_T) \cdot \epsilon_{\text{sg}} \cdot \epsilon_{\text{vp}}}, \quad (2)$$

where $N_{Y(nS)}^{\text{fit}}$ is the fitted number of $Y(nS)$ events from the dimuon invariant mass distribution in a p_T bin for the selected $|y|$ range, $\epsilon_{\mu\mu}$ is the dimuon efficiency, L is the integrated luminosity, \mathcal{A} is the polarization-corrected acceptance, ϵ_{sg} is the efficiency of the seagull selection, and ϵ_{vp} is the efficiency of the dimuon vertex χ^2 probability requirement. The efficiency and acceptance determinations are described below.

3.1 Efficiency factors

The dimuon efficiency for a given event is parameterized as:

$$\epsilon_{\mu\mu} \equiv \epsilon_1[p_T(\mu_1), \eta(\mu_1)] \cdot \epsilon_2[p_T(\mu_2), \eta(\mu_2)] \cdot \rho, \quad (3)$$

where $\epsilon_i[p_T(\mu_i), \eta(\mu_i)]$ is the overall single-muon quality and trigger efficiency. The kinematic dependence of the ρ factor was determined in a study based on Monte Carlo (MC) simulation using EVTGEN [19] with a detector simulation performed with GEANT4 [20]. The parameter ρ accounts for the possibility that two genuine muons can be merged during the reconstruction or trigger selection, causing an inefficiency. It was found to depend on the quadrature sum of the difference in p_T , η , and ϕ between the two muons. The MC simulation result was validated by measuring the ρ factor with $Y(nS)$ events reconstructed using a data set that required only a single-muon trigger.

The single-muon efficiencies are measured using the tag-and-probe approach based on control samples in data, as described in Ref. [21], times the tracking efficiency (0.99 ± 0.01), determined from MC simulation. We assume that the dimuon efficiency within each $Y(nS)$ mass region is the same for signal and background. The dimuon efficiency $\epsilon_{\mu\mu}$ for a given $(p_T, |y|)$ is obtained by averaging the calculated event dimuon efficiency $\epsilon_{\mu\mu}$ for each data event in the bin. This is done separately for the three Y states, using a mass range of ± 200 MeV for the $Y(1S)$ and ± 100 MeV for the higher-mass states. The narrower range for the $Y(2S)$ and $Y(3S)$ states is chosen because of the closeness in mass of these two states. To determine ϵ_{sg} , we note that there is a 50% probability that a $Y(nS)$ state will decay in the seagull configuration. It was verified in MC simulation that $\epsilon_{sg} = 0.5$. The efficiency ϵ_{vp} for the dimuon vertex fit χ^2 probability requirement is determined to be 0.99 ± 0.01 from MC simulation, where the uncertainty is statistical. This efficiency was validated in data using events from a trigger that did not require vertex selection.

3.2 Acceptance

For each $Y(nS)$ state the acceptance \mathcal{A} is computed in each $(p_T, |y|)$ bin and defined as the fraction of its dimuon decays that satisfy the single-muon kinematic selections given by Eq. (1). The acceptances are computed using generator-level muons, then repeated using reconstructed muons in the full simulation study. The results agree to better than 2% at all p_T values. To account for the effect of the $Y(nS)$ polarization on the muon angular distribution, each MC simulation event is weighted by an angular factor w :

$$w = \frac{3}{4\pi} \frac{1}{3 + \lambda_\theta} (1 + \lambda_\theta \cos^2 \theta + \lambda_\phi \sin^2 \theta \cos 2\phi + \lambda_{\theta\phi} \sin 2\theta \cos \phi), \quad (4)$$

where λ_θ , λ_ϕ , $\lambda_{\theta\phi}$ are the measured polarization parameters [5], θ is the polar angle, and ϕ the azimuthal angle of the positively charged muon in the $Y(nS)$ helicity frame (HX). The polarization was measured in the range $10 < p_T < 50$ GeV in the same two rapidity bins as this analysis. The measured polarization parameters do not show a statistically significant dependence on p_T . We linearly interpolate each of the measured polarization parameters in p_T . Linear interpolation is also used for the 68.3% confidence level (CL) uncertainties in the polarization measurements to determine the uncertainty in the three parameters from the analysis. The polarization parameters for $p_T > 50$ GeV are taken to be the average of the measured values for $10 < p_T < 50$ GeV. The largest measured absolute uncertainty for each parameter is used for the extrapolated uncertainties because the spread in nominal values is small. The acceptance is computed initially using a flat p_T distribution within a bin, then reweighted after fitting the measured p_T distribution to a functional form (see Section 5). The acceptances in each p_T bin for the three rapidity intervals are given in Appendix A (Tables 8–16) for the measured polarization central value and the 68.3% CL uncertainties on the parameters [5]. In addition, we report the acceptance computed for the hypotheses of zero, 100% transverse, and 100% longitudinal polarization that correspond to the parameter values $\lambda_\phi = \lambda_{\theta\phi} = 0$ and $\lambda_\theta = 0, +1$, and -1 .

respectively. Because of the agreement in the acceptance when computed with generator-level and reconstructed muons, the cross section results reported here can be scaled to accommodate any other polarization by using a generator-level MC simulation with a given polarization.

4 Yield determination procedure

4.1 Lineshape determination

The $Y(nS)$ lineshape is determined using the measured muon momenta and their uncertainties, along with a generator-level simulated invariant mass (SIM) distribution including final-state radiation (FSR) effects. For events in a given $(p_T, |y|)$ bin, the distribution of the dimuon invariant mass uncertainty ζ is computed from the muon track error matrices.

In order to describe the $Y(nS)$ SIM distribution without detector resolution effects, we simulate dimuon events for a given $Y(nS)$ state using EVTGEN and compute the FSR using PHOTOS [22, 23]. The standard PHOTOS minimum photon energy for the $Y(nS)$ states is ≈ 50 MeV, which is of the same order as our dimuon invariant mass uncertainty. To improve the description, we extend the photon energy spectrum down to 2 MeV using a fit of the SIM distribution to the QED inner-bremsstrahlung formula [23].

In each rapidity range, the $Y(nS)$ lineshape for a given p_T bin is expressed by a probability density function (PDF) for the signal dimuon mass $M_{\mu\mu}$. This function $\mathcal{F}(M_{\mu\mu}; c_w, \delta m)$ is the average of N values of the dimuon mass m_i smeared with a resolution ζ_i :

$$\mathcal{F}(M_{\mu\mu}; c_w, \delta m) = \frac{1}{N} \sum_{i=1}^N \frac{1}{\sqrt{2\pi}c_w\zeta_i} e^{-(M_{\mu\mu}-m_i-\delta m)^2/2c_w^2\zeta_i^2}. \quad (5)$$

Each $Y(nS)$ state is handled in the same fashion. Values of m_i and ζ_i are selected by randomly sampling the radiative mass function and the ζ distribution for that $(p_T, |y|)$ bin. Two correction factors are common to all three $Y(nS)$ peaks in a given $(p_T, |y|)$ bin: a width scale factor c_w , to correct for any ζ scale difference between data and the MC simulation, and a mass-shift δm , to correct for any difference in p_T scale between data and the MC simulation. We sample $N = 25000$ (m_i, ζ_i) points per p_T bin, stored in a histogram with 0.25 MeV bins to smooth the fluctuations and retain shape features. This histogram gives the normalized, resolution-smeared mass PDF for a given $Y(nS)$ state in a particular $(p_T, |y|)$ bin. The procedure was validated in MC simulation by generating the lineshape using a subset of generated $Y(1S)$ events, then fitting the rest of the events with that lineshape. The fitted number of events was consistent with the generated number.

4.2 Fitting for yields

To determine the yields of the three states in each p_T and $|y|$ range requires a fit to the dimuon mass distribution in every $(p_T, |y|)$ bin. The total PDF for $M_{\mu\mu}$ describes the signal and background contributions to the dimuon invariant mass distribution using a signal PDF as defined in Eq. (5) for each of the $Y(nS)$ states, plus a background function. Four background functions are studied: an exponential and a Chebyshev series with maximum order of 0, 1, or 2.

We measure the yield by performing an extended maximum-likelihood fit using ROOFIT [24] to determine the number of signal events associated with each normalized signal PDF. To allow cancellation of some common uncertainties in the muon acceptance and efficiency calculation in the measurement of the ratios of $Y(2S)$ and $Y(3S)$ differential cross sections to that of the $Y(1S)$, we perform an additional fit normalized to the $Y(1S)$ yield. For each p_T bin the optimal

background function is determined using the Akaike Information Criterion (AIC) [25], taking the function with the largest relative probability, as discussed in Ref. [26]. This method is similar to a maximum-likelihood evaluation, but it adds a term equal to twice the number of free parameters in the fit, thus penalizing addition of free parameters. The fit determines the parameters c_w and δm for each p_T bin. The fit correlation matrix shows that their influence on the yields is a small fraction of the statistical uncertainty in each yield.

The plots in Fig. 1 show two examples of fitting the dimuon invariant mass distribution using the lineshape method. The lower plots show the pull, $(N_{\text{data}} - N_{\text{fit}})/\sigma_{\text{data}}$, in each dimuon mass bin, where N_{data} is the observed number of events in the bin, N_{fit} is the integral of the fitted signal and background function in that bin, and the uncertainty σ_{data} is the Poisson statistical uncertainty. As can be seen in Fig. 1, the lineshape description represents the data well, even at high p_T and large rapidity.

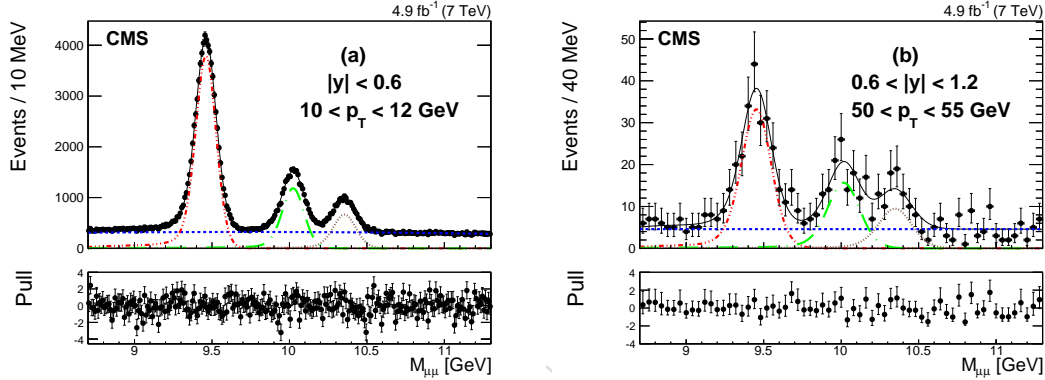


Figure 1: Results of the fits to the dimuon invariant mass distribution for events in two bins: (a): $|y| < 0.6$, $10 < p_T < 12$ GeV and (b): $0.6 < |y| < 1.2$, $50 < p_T < 55$ GeV. The solid line is the result of the full fit. The dash-dotted line is the Y(1S) signal fit, the long-dashed line is the Y(2S) signal fit, and the dotted line is the Y(3S) signal fit. The short-dashed line is the background contribution. The lower plots show the pull for each mass bin.

4.3 Systematic uncertainties

The overall systematic uncertainty in the cross section for a given $(p_T, |y|)$ bin includes uncertainties from the background fit method, the lineshape determination, the dimuon efficiency, the acceptance variations due to varying the polarization parameters within their 68.3% CL ranges, and the integrated luminosity. The systematic uncertainty from the background function is estimated using the maximum difference in yields among background functions with an AIC probability above 5% [25, 26] relative to the best background choice. An upper limit of 1% on the systematic uncertainty from the lineshape function determination for all three Y(nS) states and all $(p_T, |y|)$ bins is estimated by varying the width of the mass region in which the mass resolution parameter ζ is determined. The efficiency systematic is evaluated by modifying $\epsilon_{\mu\mu}$ event by event, using the ± 1 standard deviation values from the tag-and-probe measurements [5]. There is a 1% systematic uncertainty to account for small variations in $\epsilon_{\mu\mu}$ as a function of $M_{\mu\mu}$ observed in the data. The measured ρ factor values from the experimental determination and from MC simulation agree over the full p_T range. We assign a systematic uncertainty for ρ of 0.5–5%, which equals the full difference between the MC simulation and the experimental measurement. We compute the acceptance systematic uncertainty by raising and lowering all three polarization parameters by their interpolated 68.3% CL values from Ref. [5]. The resulting 5–8% change in the acceptance is used as the systematic uncertainty in the acceptance as tabulated in Appendix A (Tables 8–16). The total systematic uncertainty is

found from the quadrature sum of the individual systematic uncertainties. It is comparable to or smaller than the statistical uncertainty for $p_T > 40$ GeV. There is a 2.2% uncertainty [27] from the integrated luminosity determination that applies to all p_T bins. This uncertainty is not included in the uncertainties displayed in the figures or given in the tables.

5 Results

The measured $Y(nS)$ differential cross sections versus p_T are shown in Fig. 2 over the full rapidity range $|y| < 1.2$. The vertical bars on the points in Fig. 2 show the statistical and systematic uncertainties added in quadrature. Earlier CMS measurements [2] are shown for comparison, scaled by 0.5 to account for the smaller $|y|$ range in the latest measurement, where the scaling assumes that the rapidity distribution is flat. The $Y(nS)$ differential cross sections peak near $p_T = 4$ GeV, as seen in Fig. 2. Their shape can be described by an exponential function for $10 \lesssim p_T \lesssim 20$ GeV, while for $p_T \gtrsim 20$ GeV the data lie above the exponential and the slope changes. Therefore, we fit the high- p_T measurements for each $Y(nS)$ state using a power-law parametrization:

$$\left. \frac{d\sigma(\text{pp} \rightarrow Y(nS))}{dp_T} \right|_{|y|\text{range}} \times \mathcal{B}(Y(nS) \rightarrow \mu^+ \mu^-) = \frac{A}{C + (\frac{p_T}{p_0})^\alpha}, \quad (6)$$

where A is a normalization with units of pb/GeV. The value of p_0 is fixed to 20 GeV and has no influence on the exponent α , which describes the curvature of the function. The differential cross section fits are evaluated using the bin-integral method and the results are given in Table 1. The bin centers are determined by the functional-weight method described in [28], using the exponential fit for $p_T < 20$ GeV and the power-law form in Eq. 6 for $p_T > 20$ GeV. Shifts from the p_T -weighted mean values are negligible in all except the highest- p_T bin, where using the functional weight moves the bin center from 79 to 82 GeV. Tables 2-4 in Appendix A give the measured values shown in Fig. 2 as well as for the two rapidity ranges $|y| < 0.6$ and $0.6 < |y| < 1.2$. As the values of α in Table 1 show, the p_T dependence of $Y(3S)$ production is significantly harder than that of the $Y(1S)$ and $Y(2S)$.

To illustrate the quality of this functional description, Fig. 2 (b) shows the fit results for the $Y(1S)$ state with $|y| < 1.2$. The solid line is the power-law fit for $p_T > 20$ GeV. The dashed line is the exponential fit for $10 < p_T < 20$ GeV. The lower plot shows, for each p_T bin, the pull determined from the differential cross section value in a $(p_T, |y|)$ bin and its total uncertainty.

Table 1: The values of the parameters in Eq. (6) from the power-law fit to $Y(1S)$ events with $p_T > 20$ GeV and $|y| < 1.2$, along with the χ^2 value and the number of degrees of freedom n_d .

	Y(1S)	Y(2S)	Y(3S)
A	14.00 ± 0.75	6.88 ± 0.48	4.01 ± 0.30
α	5.75 ± 0.07	5.62 ± 0.10	5.26 ± 0.10
C	0.45 ± 0.13	0.62 ± 0.18	0.26 ± 0.15
χ^2	8.7	11	15
n_d	14	14	14

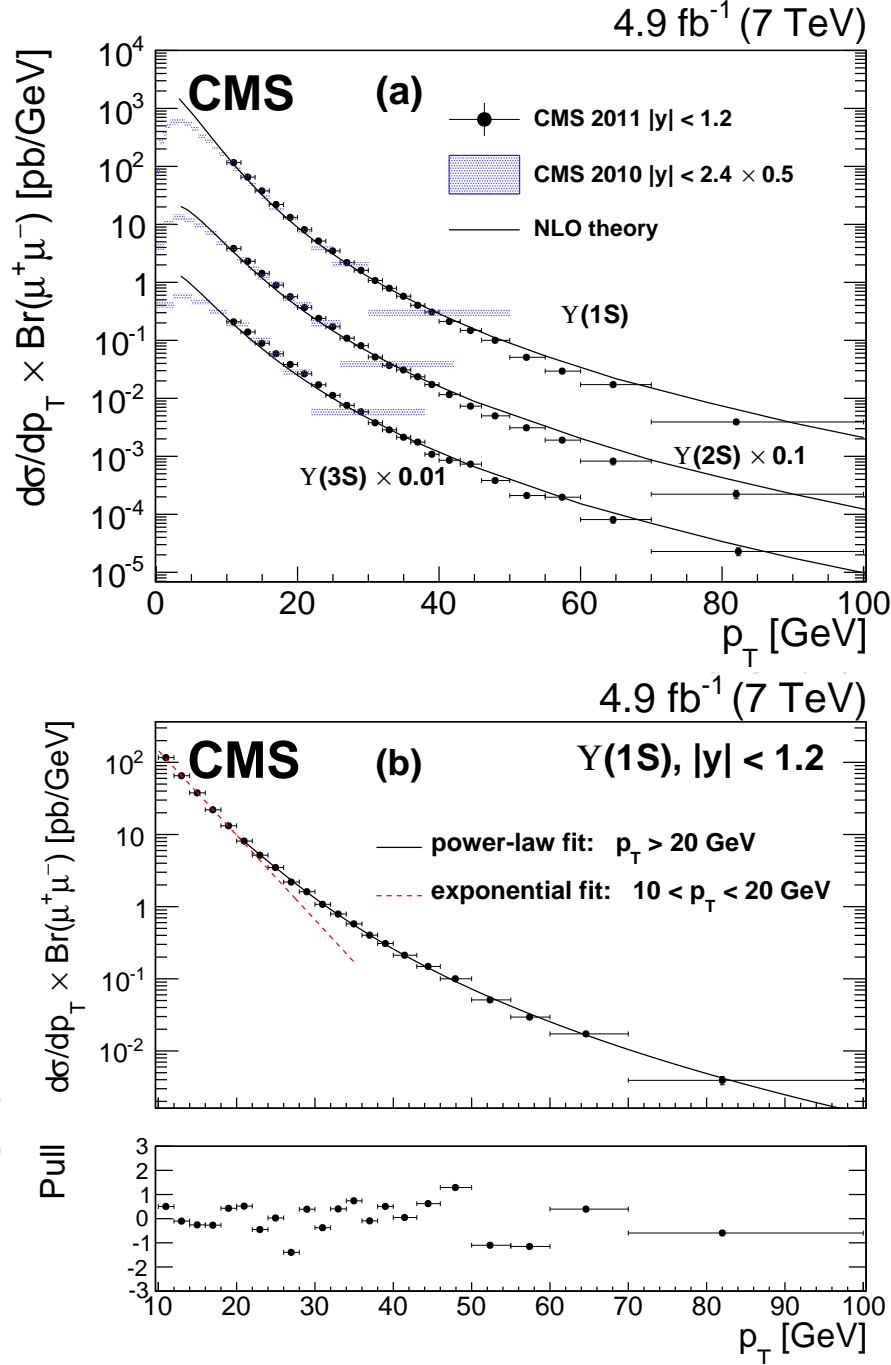


Figure 2: (a) The $Y(nS)$ differential p_T cross sections times dimuon branching fractions for $|y| < 1.2$. The $Y(2S)$ and $Y(3S)$ measurements are scaled by 0.1 and 0.01, respectively, for display purposes. The vertical bars show the total uncertainty, excluding the systematic uncertainty in the integrated luminosity. The horizontal bars show the bin widths. Previous CMS measurements for $|y| < 2.4$ are shown as cross-hatched areas [2]. These results have been scaled by 0.5 to account for the smaller $|y|$ range in the latest measurement, where the scaling assumes that the rapidity distribution is flat. The solid lines are the NLO calculations from Ref. [13] extended by the authors to cover the range $p_T < 100$ GeV. (b) Details of the parametrized cross section fit described in the text for $Y(1S)$ with $|y| < 1.2$. In this plot the solid line is the result of the power-law fit (see Eq. 6) for $p_T > 20$ GeV. The dashed line shows an exponential fit to the data for $10 < p_T < 20$ GeV. The lower plot shows the pulls of the fit as defined in the text.

Next, we consider the p_T dependence of the ratios of the $Y(nS)$ production cross sections times their dimuon branching fractions. The yield fits are redone to compute explicitly the yield ratio r_{21} for $Y(2S)$ to $Y(1S)$ and r_{31} for $Y(3S)$ to $Y(1S)$. The efficiency ratio is computed for each $(p_T, |y|)$ bin. The polarization-weighted acceptance and its uncertainty is computed for each state separately, and the uncertainties are added in quadrature to determine the uncertainty in the ratio. The corrected yield ratios are $R_{n1}(p_T, |y|) = r_{n1}(p_T, |y|) (\mathcal{A}_1 \epsilon_1) / (\mathcal{A}_n \epsilon_n)$, where $n = 2, 3$. The measured corrected ratios are shown in Fig. 3 and given in Appendix A (Tables 5–7). The rapid rise of both ratios for $p_T < 20$ GeV slows significantly for $p_T \gtrsim 20$ GeV. The curves on the ratio plots are the ratios of the corresponding fitted functions from the individual $Y(nS)$ differential cross section fits (exponential for $p_T < 20$ GeV, power-law for $p_T > 20$ GeV). The curves confirm that the change in ratios occurs in the same p_T range in which $d\sigma/dp_T$ also changes behavior.

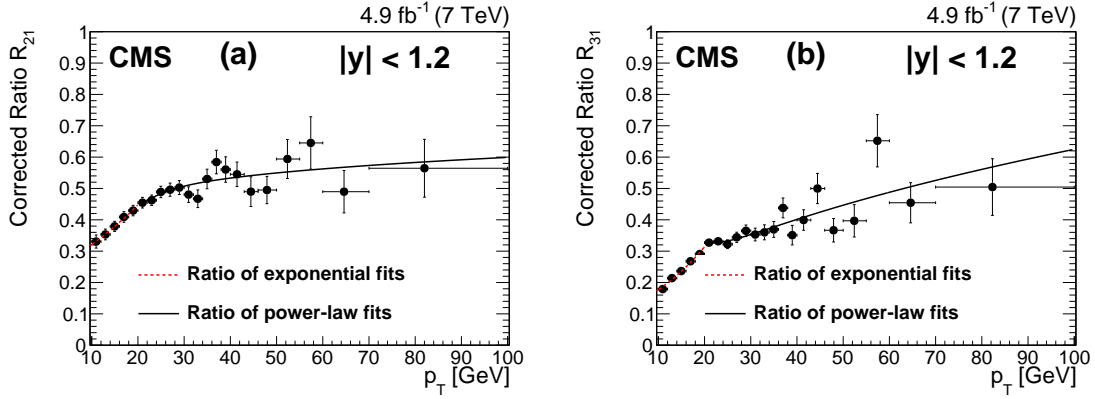


Figure 3: Measured differential cross section ratios as a function of p_T . Corrected yield ratios: (a) R_{21} ; (b) R_{31} . The dashed line is the ratio of the exponential fits to the individual differential cross sections for $10 < p_T < 20$ GeV. The solid line is the ratio of the corresponding power-law fits for $p_T > 20$ GeV.

6 Discussion

Theoretical predictions for the $Y(nS)$ differential cross sections have been previously compared to the first LHC cross section measurements [10, 14, 15]. A more recent CMS measurement [2] included the currently available predictions from the CSM [14], valid for $p_T < 35$ GeV, and an unpublished NRQCD prediction that covers the range $p_T < 30$ GeV. The NRQCD + NLO analysis from Ref. [13] describes $Y(nS)$ production at Tevatron and LHC energies for $p_T < 50$ GeV. An extension of these predictions to $p_T = 100$ GeV is compared to the CMS measurements in Fig. 2 (a). The calculations describe the trends of the data for all three $Y(nS)$ states, including the feature that the $Y(3S)$ p_T spectrum is harder than those of the two lower-mass states.

The color evaporation model (CEM), a variant of the CSM, predicts that above a minimum $p_T \approx M_{Y(1S)}$, all bottomonium states should have the same p_T dependence [29]. The measured ratios of the differential cross sections as a function of p_T in Fig. 3 show that this is not the case for p_T less than about 40 GeV.

Changing the $Y(nS)$ p_T threshold for the data used in calculating the NRQCD predictions results in different LDMEs [10, 30, 31]. Recent theoretical work [12, 16] has demonstrated the impact of varying the p_T thresholds in NRQCD analyses to study different production amplitude behavior. These new CMS data provide a significant extension of the p_T range that can be used in evaluating matrix elements and studying p_T -dependent corrections in NRQCD and

other models. The new results on $Y(3S)$ production are sufficiently accurate to allow one to focus model building of the p_T behavior on that state, for which feeddown contributions come only from the $\chi_b(3P)$.

7 Summary

Measurements of the differential production cross sections as a function of p_T for the $Y(1S)$, $Y(2S)$, and $Y(3S)$ states in pp collisions at $\sqrt{s} = 7$ TeV have been presented, based on a data sample corresponding to an integrated luminosity of 4.9 fb^{-1} collected by the CMS experiment at the LHC. Not only do these measurements significantly improve the precision of the results in previously analyzed p_T ranges [1–3], they also extend the maximum p_T range from 70 to 100 GeV. Evidence has been presented for the first time of the power-law nature of the p_T distributions for all three $Y(nS)$ states at high p_T . Combined with the CMS $Y(nS)$ polarization results [5], the new bottomonium measurements are a formidable challenge to our theoretical understanding of the production of heavy-quark bound states.

Acknowledgments

We congratulate our colleagues in the CERN accelerator departments for the excellent performance of the LHC and thank the technical and administrative staffs at CERN and at other CMS institutes for their contributions to the success of the CMS effort. In addition, we gratefully acknowledge the computing centres and personnel of the Worldwide LHC Computing Grid for delivering so effectively the computing infrastructure essential to our analyses. Finally, we acknowledge the enduring support for the construction and operation of the LHC and the CMS detector provided by the following funding agencies: BMWF and FWF (Austria); FNRS and FWO (Belgium); CNPq, CAPES, FAPERJ, and FAPESP (Brazil); MES (Bulgaria); CERN; CAS, MoST, and NSFC (China); COLCIENCIAS (Colombia); MSES and CSF (Croatia); RPF (Cyprus); MoER, SF0690030s09 and ERDF (Estonia); Academy of Finland, MEC, and HIP (Finland); CEA and CNRS/IN2P3 (France); BMBF, DFG, and HGF (Germany); GSRT (Greece); OTKA and NIH (Hungary); DAE and DST (India); IPM (Iran); SFI (Ireland); INFN (Italy); NRF and WCU (Republic of Korea); LAS (Lithuania); MOE and UM (Malaysia); CINVESTAV, CONACYT, SEP, and UASLP-FAI (Mexico); MBIE (New Zealand); PAEC (Pakistan); MSHE and NSC (Poland); FCT (Portugal); JINR (Dubna); MON, RosAtom, RAS and RFBR (Russia); MESTD (Serbia); SEIDI and CPAN (Spain); Swiss Funding Agencies (Switzerland); NSC (Taipei); ThEPCenter, IPST, STAR and NSTDA (Thailand); TUBITAK and TAEK (Turkey); NASU and SFFR (Ukraine); STFC (United Kingdom); DOE and NSF (USA).

Individuals have received support from the Marie-Curie programme and the European Research Council and EPLANET (European Union); the Leventis Foundation; the A. P. Sloan Foundation; the Alexander von Humboldt Foundation; the Belgian Federal Science Policy Office; the Fonds pour la Formation à la Recherche dans l'Industrie et dans l'Agriculture (FRIA-Belgium); the Agentschap voor Innovatie door Wetenschap en Technologie (IWT-Belgium); the Ministry of Education, Youth and Sports (MEYS) of Czech Republic; the Council of Science and Industrial Research, India; the Compagnia di San Paolo (Torino); the HOMING PLUS programme of Foundation for Polish Science, cofinanced by EU, Regional Development Fund; and the Thalís and Aristeia programmes cofinanced by EU-ESF and the Greek NSRF.

8 Appendix A

Table 2: The p_T bin width, the weighted mean p_T within a bin, and the differential cross section times the dimuon branching fraction: $\frac{d\sigma}{p_T} \times \text{Br}(Y(nS) \rightarrow \mu^+\mu^-)$ for the $Y(1S)$, $Y(2S)$, and $Y(3S)$ with $0 < |y| < 0.6$. The statistical uncertainty in the differential cross section is given as the percentage of the cross section in the format: $\frac{\sigma_{\text{stat}}}{d\sigma/dp_T} (\%)$ and similarly for the systematic uncertainty. The percentage systematic uncertainty for a negative systematic shift is given in parentheses. The statistical uncertainties are derived from the fit to the dimuon mass spectrum. The systematic uncertainties are discussed in the text. The 2.2% systematic uncertainty in the integrated luminosity is not included.

		Y(1S)			Y(2S)			Y(3S)		
p_T	$\langle p_T \rangle$	$\frac{d\sigma}{dp_T} \cdot B$	$\frac{\sigma_{\text{stat}}}{d\sigma/dp_T}$	$\frac{\sigma_{\text{syst}}}{d\sigma/dp_T}$	$\frac{d\sigma}{dp_T} \cdot B$	$\frac{\sigma_{\text{stat}}}{d\sigma/dp_T}$	$\frac{\sigma_{\text{syst}}}{d\sigma/dp_T}$	$\frac{d\sigma}{dp_T} \cdot B$	$\frac{\sigma_{\text{stat}}}{d\sigma/dp_T}$	$\frac{\sigma_{\text{syst}}}{d\sigma/dp_T}$
GeV	GeV	(fb/GeV)	(%)	(%)	(fb/GeV)	(%)	(%)	(fb/GeV)	(%)	(%)
10–12	11.0	60936	0.5	6.8 (7.2)	20036	1.0	8.6 (9.4)	10951	1.4	10.0 (11.3)
12–14	13.0	33828	0.5	5.1 (5.6)	12072	1.1	6.0 (6.7)	7181	1.4	7.1 (8.0)
14–16	15.0	19670	0.6	4.8 (5.2)	7621	1.2	5.2 (5.7)	4596	1.6	5.7 (6.3)
16–18	17.0	11504	0.8	4.6 (4.9)	4858	1.3	5.1 (5.5)	3097	1.7	5.6 (6.1)
18–20	19.0	6914	0.9	4.5 (4.7)	3034	1.5	4.9 (5.2)	1966	2.0	5.2 (5.6)
20–22	21.0	4235	1.1	4.2 (4.4)	1932	1.8	4.6 (4.9)	1423	2.2	5.0 (5.2)
22–24	23.0	2721	1.4	4.1 (4.3)	1203	2.3	4.5 (4.6)	893	2.7	4.7 (4.9)
24–26	25.0	1848	1.7	4.1 (4.2)	849	2.6	4.6 (4.7)	594	3.3	4.9 (5.1)
26–28	27.0	1117	2.2	4.3 (4.4)	537	3.6	5.7 (5.8)	381	4.4	6.1 (6.2)
28–30	29.0	845	2.5	4.4 (4.5)	413	4.0	5.8 (5.8)	314	4.7	6.0 (6.1)
30–32	31.0	593	2.8	4.3 (4.4)	288	4.4	5.0 (5.1)	209	5.2	5.0 (5.2)
32–34	33.0	420	3.5	4.7 (4.8)	194	6.0	6.7 (6.8)	162	6.5	6.4 (6.5)
34–36	35.0	314	3.8	4.6 (4.6)	158	5.8	5.9 (6.0)	112	7.1	5.7 (5.8)
36–38	37.0	209	4.8	4.5 (4.6)	123	6.5	4.6 (4.7)	92	7.5	4.6 (4.7)
38–40	39.0	157	5.4	4.2 (4.2)	86	7.8	4.4 (4.6)	61	9.5	4.6 (4.7)
40–43	41.4	114	5.0	4.0 (4.1)	61	7.6	4.3 (4.4)	42	9.3	4.4 (4.6)
43–46	44.4	76	6.3	5.8 (5.8)	36	10.0	9.5 (9.5)	39	9.4	7.8 (7.9)
46–50	47.9	49	6.6	4.2 (4.2)	27	9.6	4.8 (4.9)	22	10.9	5.1 (5.3)
50–55	52.4	24	9.2	5.9 (5.8)	17	10.9	4.8 (4.9)	12	13.6	4.4 (4.6)
55–60	57.4	15	11.0	6.3 (6.2)	9.8	14.8	5.0 (5.1)	8.5	15.5	4.6 (4.8)
60–70	64.6	9.2	10.1	6.6 (6.5)	4.7	15.7	7.3 (7.3)	4.9	14.8	6.0 (6.1)
70–100	82.0	2.3	12.6	11.9 (11.8)	1.2	17.6	8.9 (8.9)	1.0	19.1	7.3 (7.2)

Table 3: The p_T bin width, the weighted mean p_T within a bin, and the differential cross section times the dimuon branching fraction: $\frac{d\sigma}{dp_T} \times \text{Br}(Y(nS) \rightarrow \mu^+ \mu^-)$ for the $Y(1S)$, $Y(2S)$, and $Y(3S)$ with $0.6 < |y| < 1.2$. The notation is the same as for Table 2.

		Y(1S)			Y(2S)			Y(3S)		
p_T	$\langle p_T \rangle$	$\frac{d\sigma}{dp_T} \cdot B$	$\frac{\sigma_{\text{stat}}}{d\sigma/dp_T}$	$\frac{\sigma_{\text{syst}}}{d\sigma/dp_T}$	$\frac{d\sigma}{dp_T} \cdot B$	$\frac{\sigma_{\text{stat}}}{d\sigma/dp_T}$	$\frac{\sigma_{\text{syst}}}{d\sigma/dp_T}$	$\frac{d\sigma}{dp_T} \cdot B$	$\frac{\sigma_{\text{stat}}}{d\sigma/dp_T}$	$\frac{\sigma_{\text{syst}}}{d\sigma/dp_T}$
GeV	GeV	(fb/GeV)	(%)	(%)	(fb/GeV)	(%)	(%)	(fb/GeV)	(%)	(%)
10–12	11.0	55260	0.5	6.1 (6.3)	18371	1.2	7.8 (8.2)	9855	1.6	8.9 (10.0)
12–14	13.0	31331	0.6	4.1 (4.2)	10973	1.1	4.9 (5.2)	6741	1.5	5.5 (6.0)
14–16	15.0	18063	0.7	3.8 (4.0)	6685	1.5	4.6 (4.8)	4298	2.0	5.5 (5.7)
16–18	17.0	10481	0.9	3.8 (3.9)	4105	1.7	4.9 (5.1)	2759	2.3	4.8 (5.0)
18–20	19.0	6286	1.1	3.7 (3.8)	2624	2.1	4.6 (4.8)	1871	2.6	4.6 (4.7)
20–22	21.0	3875	1.4	3.8 (3.9)	1746	2.4	4.7 (4.8)	1220	3.0	5.0 (5.2)
22–24	23.0	2439	1.6	3.6 (3.7)	1188	2.4	3.8 (3.9)	819	3.0	4.0 (4.2)
24–26	25.0	1633	1.9	3.8 (3.9)	865	2.8	4.0 (4.1)	530	3.7	4.0 (4.2)
26–28	27.0	1080	2.2	3.8 (3.9)	551	3.4	4.5 (4.5)	377	4.3	4.7 (4.8)
28–30	29.0	765	2.5	3.7 (3.8)	397	3.9	3.9 (4.0)	274	5.0	4.2 (4.3)
30–32	31.0	484	3.8	5.0 (5.1)	229	6.5	9.0 (9.0)	170	7.8	10.3 (10.3)
32–34	33.0	371	3.7	6.0 (6.1)	175	6.0	9.8 (9.8)	123	7.8	10.3 (10.4)
34–36	35.0	263	4.3	3.7 (3.8)	151	6.1	4.0 (4.1)	101	8.1	4.3 (4.4)
36–38	37.0	193	4.9	3.6 (3.7)	113	7.0	3.9 (4.0)	84	8.6	4.3 (4.4)
38–40	39.0	152	5.7	3.7 (3.8)	87	8.1	4.0 (4.1)	47	11.9	4.2 (4.3)
40–43	41.4	98	6.0	5.0 (5.0)	55	8.4	4.3 (4.4)	43	9.8	4.2 (4.3)
43–46	44.4	73	6.5	7.1 (7.1)	37	10.3	9.9 (9.9)	34	11.1	13.4 (13.4)
46–50	47.9	51	6.7	4.0 (4.0)	23	11.0	3.9 (4.0)	16	14.2	4.0 (4.2)
50–55	52.4	27	8.6	5.1 (5.1)	14	13.2	4.5 (4.5)	8.7	18.3	4.0 (4.2)
55–60	57.4	15	11.2	5.1 (5.0)	9.2	15.5	4.6 (4.6)	11	13.7	4.5 (4.7)
60–70	64.6	8.1	10.8	5.6 (5.6)	3.6	19.7	5.1 (5.1)	3.3	20.9	5.2 (5.3)
70–100	82.0	1.6	15.0	7.4 (7.2)	1.0	24.0	7.0 (6.9)	1.3	19.8	6.6 (6.7)

Table 4: The p_T bin width, the weighted mean p_T within a bin, and the differential cross section times the dimuon branching fraction: $\frac{d\sigma}{dp_T} \times \text{Br}(Y(nS) \rightarrow \mu^+ \mu^-)$ for the $Y(1S)$, $Y(2S)$, and $Y(3S)$ with $0 < |y| < 1.2$. The notation is the same as for Table 2.

		Y(1S)			Y(2S)			Y(3S)		
p_T	$\langle p_T \rangle$	$\frac{d\sigma}{dp_T} \cdot B$	$\frac{\sigma_{\text{stat}}}{d\sigma/dp_T}$	$\frac{\sigma_{\text{syst}}}{d\sigma/dp_T}$	$\frac{d\sigma}{dp_T} \cdot B$	$\frac{\sigma_{\text{stat}}}{d\sigma/dp_T}$	$\frac{\sigma_{\text{syst}}}{d\sigma/dp_T}$	$\frac{d\sigma}{dp_T} \cdot B$	$\frac{\sigma_{\text{stat}}}{d\sigma/dp_T}$	$\frac{\sigma_{\text{syst}}}{d\sigma/dp_T}$
GeV	GeV	(fb/GeV)	(%)	(%)	(fb/GeV)	(%)	(%)	(fb/GeV)	(%)	(%)
10–12	11.0	116415	0.4	6.4 (6.7)	38540	0.7	8.1 (8.7)	20882	1.1	9.3 (10.5)
12–14	13.0	65266	0.4	4.6 (4.9)	23088	0.8	5.4 (5.9)	13947	1.0	6.2 (6.9)
14–16	15.0	37778	0.5	4.3 (4.6)	14321	0.9	4.7 (5.1)	8909	1.3	5.2 (5.7)
16–18	17.0	22008	0.6	4.1 (4.4)	8969	1.1	4.7 (5.0)	5873	1.4	5.0 (5.3)
18–20	19.0	13212	0.7	4.1 (4.2)	5665	1.3	4.6 (4.8)	3842	1.6	4.7 (5.0)
20–22	21.0	8116	0.9	4.0 (4.1)	3683	1.5	4.4 (4.6)	2648	1.8	4.7 (4.9)
22–24	23.0	5162	1.0	3.9 (4.0)	2393	1.7	4.1 (4.2)	1713	2.0	4.3 (4.5)
24–26	25.0	3483	1.3	3.9 (4.0)	1715	1.9	4.2 (4.3)	1124	2.4	4.4 (4.5)
26–28	27.0	2197	1.5	4.0 (4.0)	1089	2.5	4.6 (4.7)	759	3.1	4.9 (5.0)
28–30	29.0	1611	1.8	4.0 (4.1)	811	2.8	4.6 (4.7)	588	3.4	4.8 (5.0)
30–32	31.0	1077	2.3	4.2 (4.3)	517	3.8	5.7 (5.7)	380	4.5	6.2 (6.3)
32–34	33.0	791	2.5	4.7 (4.7)	369	4.2	6.5 (6.6)	286	5.0	6.5 (6.6)
34–36	35.0	577	2.8	4.1 (4.1)	309	4.2	4.7 (4.7)	213	5.3	4.8 (4.9)
36–38	37.0	402	3.4	4.0 (4.1)	236	4.8	4.2 (4.3)	176	5.7	4.4 (4.6)
38–40	39.0	308	3.9	3.9 (3.9)	173	5.6	4.2 (4.3)	109	7.5	4.4 (4.5)
40–43	41.4	212	3.9	4.1 (4.2)	116	5.6	4.2 (4.3)	86	6.8	4.3 (4.5)
43–46	44.4	148	4.5	5.3 (5.3)	73	7.2	7.5 (7.5)	73	7.2	8.1 (8.2)
46–50	47.9	100	4.7	4.0 (4.0)	50	7.3	4.2 (4.3)	38	8.7	4.5 (4.6)
50–55	52.4	51	6.3	5.0 (5.0)	31	8.4	4.5 (4.6)	21	11.0	4.2 (4.4)
55–60	57.4	29	7.9	5.4 (5.4)	19	10.7	4.8 (4.8)	20	10.3	4.6 (4.7)
60–70	64.6	17	7.4	6.0 (5.9)	8.3	12.4	6.1 (6.1)	8.1	12.2	5.5 (5.6)
70–100	82.0	3.9	9.7	8.9 (8.8)	2.2	14.6	7.6 (7.5)	2.3	14.0	6.9 (6.9)

Table 5: The p_T bin width and corrected yield ratios R_{21} and R_{31} for $|y| < 0.6$. The statistical uncertainty in the corrected yield ratios is given as the percentage of the ratio in the format: $\frac{\sigma_{\text{stat}}}{R_{n1}} (\%)$ ($n = 2,3$) and similarly for the systematic uncertainty. The statistical uncertainties are derived from the fit to the dimuon mass spectrum. The systematic uncertainties are discussed in the text. The 2.2% systematic uncertainty in the integrated luminosity is not included.

p_T	R_{21}	$\frac{\sigma_{\text{stat}}}{R_{21}}$	$\frac{\sigma_{\text{syst}}}{R_{21}}$	R_{31}	$\frac{\sigma_{\text{stat}}}{R_{31}}$	$\frac{\sigma_{\text{syst}}}{R_{31}}$
GeV		(%)	(%)		(%)	(%)
10–12	0.33	1.0	7.2	0.18	1.4	8.6
12–14	0.36	1.1	5.9	0.21	1.5	6.7
14–16	0.39	1.3	4.9	0.23	1.7	5.5
16–18	0.42	1.4	4.7	0.27	1.8	5.2
18–20	0.44	1.7	4.1	0.28	2.1	4.6
20–22	0.46	2.1	3.8	0.34	2.4	4.2
22–24	0.44	2.6	3.4	0.33	3.0	3.8
24–26	0.46	3.0	3.4	0.32	3.6	3.8
26–28	0.48	3.9	3.9	0.34	4.6	4.5
28–30	0.49	4.4	3.8	0.37	5.0	4.1
30–32	0.49	5.1	3.5	0.35	5.8	3.6
32–34	0.46	6.4	4.1	0.39	6.9	4.1
34–36	0.50	6.8	3.6	0.36	7.8	3.7
36–38	0.59	7.8	3.3	0.44	8.6	4.0
38–40	0.55	9.2	3.1	0.39	10.6	3.5
40–43	0.54	8.8	3.0	0.37	10.3	3.3
43–46	0.48	11.4	5.3	0.51	10.9	3.9
46–50	0.55	11.3	3.1	0.45	12.3	3.5
50–55	0.72	13.4	3.2	0.51	15.6	4.6
55–60	0.66	17.4	2.9	0.57	18.2	4.8
60–70	0.51	17.8	2.5	0.53	16.9	2.8
70–100	0.53	20.3	4.1	0.44	21.9	9.1

Table 6: The p_T bin width and corrected yield ratios R_{21} and R_{31} for $0.6 < |y| < 1.2$. The notation is the same as for Table 5.

p_T	R_{21}	$\frac{\sigma_{\text{stat}}}{R_{21}}$	$\frac{\sigma_{\text{syst}}}{R_{21}}$	R_{31}	$\frac{\sigma_{\text{stat}}}{R_{31}}$	$\frac{\sigma_{\text{syst}}}{R_{31}}$
GeV		(%)	(%)		(%)	(%)
10–12	0.33	1.1	5.5	0.18	1.6	6.4
12–14	0.35	1.2	3.9	0.22	1.5	4.3
14–16	0.37	1.4	3.6	0.24	1.9	4.1
16–18	0.39	1.7	3.4	0.26	2.2	4.1
18–20	0.42	2.1	3.4	0.30	2.5	3.6
20–22	0.45	2.4	3.2	0.31	3.0	3.8
22–24	0.49	2.8	2.8	0.34	3.3	3.0
24–26	0.53	3.2	2.8	0.32	4.0	3.3
26–28	0.51	3.9	3.1	0.35	4.7	3.2
28–30	0.52	4.6	2.9	0.36	5.5	3.4
30–32	0.47	6.4	5.3	0.35	7.6	6.6
32–34	0.47	6.8	5.3	0.33	8.2	5.9
34–36	0.58	7.3	3.0	0.39	8.9	3.5
36–38	0.58	8.2	2.9	0.44	9.5	3.4
38–40	0.57	9.4	2.9	0.31	12.8	3.2
40–43	0.56	9.8	3.0	0.44	11.0	4.5
43–46	0.51	12.9	6.8	0.47	15.5	5.4
46–50	0.45	12.3	2.6	0.31	15.0	3.3
50–55	0.51	14.9	2.6	0.33	19.4	4.2
55–60	0.63	18.4	4.6	0.77	16.6	2.9
60–70	0.46	21.0	4.7	0.38	23.2	6.4
70–100	0.66	25.8	4.2	0.75	23.4	9.7

Table 7: The p_T bin width and corrected yield ratios R_{21} and R_{31} for $|y| < 1.2$. The notation is the same as for Table 5.

p_T	R_{21}	$\frac{\sigma_{\text{stat}}}{R_{21}}$	$\frac{\sigma_{\text{syst}}}{R_{21}}$	R_{31}	$\frac{\sigma_{\text{stat}}}{R_{31}}$	$\frac{\sigma_{\text{syst}}}{R_{31}}$
GeV	(%)	(%)	(%)	(%)	(%)	(%)
10–12	0.33	0.7	6.2	0.18	1.0	7.4
12–14	0.35	0.8	4.8	0.21	1.1	5.4
14–16	0.38	1.0	4.1	0.24	1.3	4.5
16–18	0.41	1.1	4.0	0.27	1.4	4.3
18–20	0.43	1.3	3.6	0.29	1.6	3.9
20–22	0.45	1.6	3.4	0.33	1.9	3.7
22–24	0.46	1.9	3.0	0.33	2.2	3.3
24–26	0.49	2.2	3.0	0.32	2.7	3.4
26–28	0.50	2.8	3.2	0.34	3.3	3.4
28–30	0.50	3.2	3.1	0.36	3.7	3.5
30–32	0.48	4.0	3.3	0.35	4.6	3.5
32–34	0.47	4.7	3.8	0.36	5.3	4.0
34–36	0.53	5.0	3.1	0.37	5.9	3.5
36–38	0.58	5.7	3.1	0.44	6.4	3.4
38–40	0.56	6.6	3.0	0.35	8.2	3.3
40–43	0.55	6.6	2.9	0.40	7.5	3.2
43–46	0.49	8.6	4.5	0.50	8.9	3.7
46–50	0.49	8.4	2.7	0.37	9.7	3.2
50–55	0.59	10.1	2.6	0.40	12.5	3.6
55–60	0.65	12.6	2.8	0.65	12.4	3.0
60–70	0.49	13.6	2.5	0.45	13.9	2.6
70–100	0.56	16.0	3.3	0.50	16.5	7.0

Table 8: The dimuon acceptance \mathcal{A} calculated using the CMS measured polarization and its positive and negative uncertainties $\mathcal{A}(\sigma^\pm)$, and the values of the acceptance assuming no polarization $\mathcal{A}(\text{unpol})$, transverse polarization $\mathcal{A}(T)$, and longitudinal polarization $\mathcal{A}(L)$ for the $Y(1S)$ state and $|y| < 0.6$.

p_T [GeV]	\mathcal{A}	$\mathcal{A}(\sigma^+)$	$\mathcal{A}(\sigma^-)$	$\mathcal{A}(\text{unpol})$	$\mathcal{A}(T)$	$\mathcal{A}(L)$
10–12	0.31	0.29	0.32	0.32	0.26	0.45
12–14	0.38	0.36	0.40	0.39	0.32	0.54
14–16	0.44	0.42	0.45	0.45	0.36	0.61
16–18	0.49	0.48	0.51	0.50	0.41	0.67
18–20	0.53	0.52	0.55	0.54	0.45	0.71
20–22	0.57	0.56	0.58	0.57	0.48	0.74
22–24	0.60	0.59	0.61	0.60	0.51	0.77
24–26	0.62	0.61	0.64	0.62	0.54	0.79
26–28	0.64	0.63	0.66	0.65	0.56	0.81
28–30	0.66	0.64	0.67	0.66	0.58	0.83
30–32	0.67	0.66	0.69	0.68	0.60	0.84
32–34	0.69	0.67	0.70	0.69	0.62	0.85
34–36	0.70	0.69	0.71	0.71	0.63	0.86
36–38	0.71	0.70	0.72	0.72	0.64	0.87
38–40	0.72	0.71	0.74	0.73	0.66	0.88
40–43	0.73	0.72	0.75	0.74	0.67	0.89
43–46	0.75	0.73	0.76	0.76	0.69	0.89
46–50	0.76	0.75	0.78	0.77	0.71	0.90
50–55	0.78	0.77	0.80	0.79	0.73	0.91
55–60	0.80	0.78	0.81	0.80	0.75	0.92
60–70	0.82	0.81	0.83	0.82	0.77	0.93
70–100	0.87	0.86	0.88	0.87	0.83	0.96

Table 9: The dimuon acceptance \mathcal{A} calculated using the CMS measured polarization and its positive and negative uncertainties $\mathcal{A}(\sigma^\pm)$, and the values of the acceptance assuming no polarization $\mathcal{A}(\text{unpol})$, transverse polarization $\mathcal{A}(T)$, and longitudinal polarization $\mathcal{A}(L)$ for the $Y(1S)$ state and $0.6 < |y| < 1.2$.

p_T [GeV]	\mathcal{A}	$\mathcal{A}(\sigma^+)$	$\mathcal{A}(\sigma^-)$	$\mathcal{A}(\text{unpol})$	$\mathcal{A}(T)$	$\mathcal{A}(L)$
10–12	0.29	0.28	0.30	0.29	0.24	0.38
12–14	0.35	0.34	0.36	0.35	0.30	0.46
14–16	0.42	0.41	0.43	0.42	0.36	0.54
16–18	0.47	0.46	0.48	0.47	0.40	0.60
18–20	0.52	0.51	0.53	0.51	0.44	0.66
20–22	0.55	0.54	0.56	0.55	0.48	0.70
22–24	0.59	0.58	0.60	0.59	0.51	0.74
24–26	0.61	0.60	0.63	0.62	0.54	0.77
26–28	0.64	0.63	0.65	0.64	0.57	0.79
28–30	0.66	0.64	0.67	0.66	0.59	0.81
30–32	0.67	0.66	0.69	0.68	0.61	0.83
32–34	0.69	0.67	0.70	0.70	0.63	0.84
34–36	0.70	0.69	0.71	0.71	0.64	0.86
36–38	0.71	0.70	0.72	0.73	0.66	0.87
38–40	0.72	0.71	0.74	0.74	0.67	0.88
40–43	0.74	0.73	0.75	0.75	0.68	0.88
43–46	0.75	0.74	0.77	0.77	0.70	0.89
46–50	0.77	0.76	0.78	0.78	0.72	0.90
50–55	0.79	0.78	0.80	0.80	0.74	0.91
55–60	0.81	0.80	0.82	0.81	0.76	0.92
60–70	0.83	0.82	0.84	0.83	0.78	0.93
70–100	0.88	0.87	0.89	0.88	0.84	0.96

Table 10: The dimuon acceptance \mathcal{A} calculated using the CMS measured polarization and its positive and negative uncertainties $\mathcal{A}(\sigma^\pm)$, and the values of the acceptance assuming no polarization $\mathcal{A}(\text{unpol})$, transverse polarization $\mathcal{A}(T)$, and longitudinal polarization $\mathcal{A}(L)$ for the $Y(1S)$ state and $|y| < 1.2$.

p_T [GeV]	\mathcal{A}	$\mathcal{A}(\sigma^+)$	$\mathcal{A}(\sigma^-)$	$\mathcal{A}(\text{unpol})$	$\mathcal{A}(T)$	$\mathcal{A}(L)$
10–12	0.30	0.28	0.31	0.30	0.25	0.42
12–14	0.37	0.35	0.38	0.37	0.31	0.50
14–16	0.43	0.42	0.44	0.43	0.36	0.57
16–18	0.48	0.47	0.49	0.48	0.41	0.64
18–20	0.52	0.51	0.54	0.53	0.45	0.68
20–22	0.56	0.55	0.57	0.56	0.48	0.72
22–24	0.59	0.58	0.61	0.59	0.51	0.75
24–26	0.62	0.61	0.63	0.62	0.54	0.78
26–28	0.64	0.63	0.65	0.64	0.56	0.80
28–30	0.66	0.64	0.67	0.66	0.58	0.82
30–32	0.67	0.66	0.69	0.68	0.60	0.84
32–34	0.69	0.67	0.70	0.70	0.62	0.85
34–36	0.70	0.69	0.71	0.71	0.64	0.86
36–38	0.71	0.70	0.72	0.72	0.65	0.87
38–40	0.72	0.71	0.74	0.73	0.66	0.88
40–43	0.74	0.72	0.75	0.75	0.68	0.88
43–46	0.75	0.74	0.77	0.76	0.70	0.89
46–50	0.77	0.76	0.78	0.78	0.71	0.90
50–55	0.79	0.77	0.80	0.79	0.73	0.91
55–60	0.80	0.79	0.81	0.81	0.75	0.92
60–70	0.82	0.81	0.84	0.83	0.78	0.93
70–100	0.87	0.86	0.89	0.88	0.83	0.96

Table 11: The dimuon acceptance \mathcal{A} calculated using the CMS measured polarization and its positive and negative uncertainties $\mathcal{A}(\sigma^\pm)$, and the values of the acceptance assuming no polarization $\mathcal{A}(\text{unpol})$, transverse polarization $\mathcal{A}(T)$, and longitudinal polarization $\mathcal{A}(L)$ for the $Y(2S)$ state and $|y| < 0.6$.

p_T [GeV]	\mathcal{A}	$\mathcal{A}(\sigma^+)$	$\mathcal{A}(\sigma^-)$	$\mathcal{A}(\text{unpol})$	$\mathcal{A}(T)$	$\mathcal{A}(L)$
10–12	0.31	0.30	0.33	0.34	0.27	0.48
12–14	0.37	0.36	0.39	0.41	0.33	0.56
14–16	0.43	0.41	0.45	0.47	0.38	0.63
16–18	0.48	0.46	0.50	0.51	0.42	0.68
18–20	0.52	0.51	0.54	0.55	0.46	0.73
20–22	0.56	0.54	0.57	0.58	0.49	0.76
22–24	0.59	0.57	0.61	0.61	0.52	0.79
24–26	0.61	0.59	0.63	0.63	0.55	0.81
26–28	0.64	0.62	0.65	0.66	0.58	0.83
28–30	0.65	0.63	0.67	0.67	0.59	0.84
30–32	0.66	0.64	0.68	0.69	0.61	0.85
32–34	0.68	0.66	0.70	0.71	0.63	0.87
34–36	0.69	0.67	0.71	0.72	0.64	0.88
36–38	0.70	0.68	0.72	0.73	0.65	0.88
38–40	0.71	0.69	0.73	0.74	0.66	0.89
40–43	0.73	0.71	0.75	0.76	0.69	0.90
43–46	0.74	0.72	0.76	0.77	0.70	0.91
46–50	0.76	0.74	0.78	0.79	0.72	0.92
50–55	0.77	0.76	0.79	0.80	0.74	0.92
55–60	0.79	0.78	0.81	0.82	0.76	0.93
60–70	0.82	0.80	0.83	0.84	0.78	0.95
70–100	0.87	0.85	0.88	0.88	0.84	0.97

Table 12: The dimuon acceptance \mathcal{A} calculated using the CMS measured polarization and its positive and negative uncertainties $\mathcal{A}(\sigma^\pm)$, and the values of the acceptance assuming no polarization $\mathcal{A}(\text{unpol})$, transverse polarization $\mathcal{A}(T)$, and longitudinal polarization $\mathcal{A}(L)$ for the $Y(2S)$ state and $0.6 < |y| < 1.2$.

p_T [GeV]	\mathcal{A}	$\mathcal{A}(\sigma^+)$	$\mathcal{A}(\sigma^-)$	$\mathcal{A}(\text{unpol})$	$\mathcal{A}(T)$	$\mathcal{A}(L)$
10–12	0.28	0.27	0.30	0.30	0.25	0.39
12–14	0.35	0.34	0.37	0.36	0.31	0.47
14–16	0.42	0.41	0.43	0.42	0.36	0.54
16–18	0.47	0.46	0.49	0.47	0.41	0.60
18–20	0.51	0.50	0.53	0.52	0.45	0.66
20–22	0.54	0.53	0.56	0.56	0.49	0.70
22–24	0.56	0.55	0.58	0.59	0.52	0.74
24–26	0.58	0.57	0.60	0.62	0.54	0.77
26–28	0.61	0.60	0.63	0.65	0.57	0.79
28–30	0.64	0.62	0.66	0.67	0.60	0.82
30–32	0.66	0.64	0.68	0.69	0.61	0.84
32–34	0.68	0.66	0.69	0.70	0.63	0.85
34–36	0.69	0.68	0.71	0.72	0.65	0.87
36–38	0.72	0.70	0.73	0.74	0.67	0.88
38–40	0.72	0.71	0.74	0.75	0.68	0.89
40–43	0.74	0.72	0.76	0.76	0.69	0.89
43–46	0.76	0.74	0.78	0.78	0.71	0.91
46–50	0.77	0.75	0.79	0.79	0.73	0.92
50–55	0.79	0.78	0.81	0.81	0.75	0.93
55–60	0.81	0.80	0.83	0.83	0.77	0.94
60–70	0.83	0.82	0.85	0.84	0.79	0.95
70–100	0.88	0.87	0.90	0.89	0.85	0.97

Table 13: The dimuon acceptance \mathcal{A} calculated using the CMS measured polarization and its positive and negative uncertainties $\mathcal{A}(\sigma^\pm)$, and the values of the acceptance assuming no polarization $\mathcal{A}(\text{unpol})$, transverse polarization $\mathcal{A}(T)$, and longitudinal polarization $\mathcal{A}(L)$ for the $Y(2S)$ state and $|y| < 1.2$.

p_T [GeV]	\mathcal{A}	$\mathcal{A}(\sigma^+)$	$\mathcal{A}(\sigma^-)$	$\mathcal{A}(\text{unpol})$	$\mathcal{A}(T)$	$\mathcal{A}(L)$
10–12	0.30	0.28	0.32	0.32	0.26	0.44
12–14	0.36	0.35	0.38	0.38	0.32	0.52
14–16	0.42	0.41	0.44	0.44	0.37	0.59
16–18	0.47	0.46	0.49	0.49	0.41	0.64
18–20	0.52	0.50	0.53	0.53	0.46	0.69
20–22	0.55	0.53	0.56	0.57	0.49	0.73
22–24	0.58	0.56	0.59	0.60	0.52	0.76
24–26	0.60	0.58	0.61	0.62	0.54	0.79
26–28	0.62	0.61	0.64	0.65	0.57	0.81
28–30	0.64	0.63	0.66	0.67	0.59	0.83
30–32	0.66	0.64	0.68	0.69	0.61	0.85
32–34	0.68	0.66	0.70	0.71	0.63	0.86
34–36	0.69	0.67	0.71	0.72	0.65	0.87
36–38	0.71	0.69	0.72	0.73	0.66	0.88
38–40	0.71	0.70	0.73	0.74	0.67	0.89
40–43	0.73	0.72	0.75	0.76	0.69	0.90
43–46	0.75	0.73	0.77	0.77	0.71	0.91
46–50	0.76	0.75	0.78	0.79	0.72	0.92
50–55	0.78	0.77	0.80	0.80	0.74	0.93
55–60	0.80	0.79	0.82	0.82	0.76	0.93
60–70	0.82	0.81	0.84	0.84	0.79	0.95
70–100	0.87	0.86	0.89	0.88	0.84	0.97

Table 14: The dimuon acceptance \mathcal{A} calculated using the CMS measured polarization and its positive and negative uncertainties $\mathcal{A}(\sigma^\pm)$, and the values of the acceptance assuming no polarization $\mathcal{A}(\text{unpol})$, transverse polarization $\mathcal{A}(T)$, and longitudinal polarization $\mathcal{A}(L)$ for the $Y(3S)$ state and $|y| < 0.6$.

p_T [GeV]	\mathcal{A}	$\mathcal{A}(\sigma^+)$	$\mathcal{A}(\sigma^-)$	$\mathcal{A}(\text{unpol})$	$\mathcal{A}(T)$	$\mathcal{A}(L)$
10–12	0.34	0.32	0.37	0.35	0.28	0.49
12–14	0.39	0.37	0.42	0.42	0.34	0.58
14–16	0.44	0.42	0.46	0.47	0.39	0.64
16–18	0.49	0.47	0.51	0.52	0.43	0.69
18–20	0.52	0.50	0.55	0.55	0.46	0.73
20–22	0.55	0.54	0.58	0.59	0.50	0.77
22–24	0.59	0.57	0.60	0.62	0.53	0.79
24–26	0.61	0.59	0.63	0.64	0.55	0.82
26–28	0.63	0.62	0.66	0.67	0.58	0.84
28–30	0.65	0.63	0.67	0.68	0.60	0.85
30–32	0.67	0.65	0.69	0.70	0.61	0.86
32–34	0.69	0.67	0.71	0.71	0.63	0.87
34–36	0.70	0.68	0.72	0.73	0.65	0.88
36–38	0.72	0.70	0.74	0.74	0.67	0.89
38–40	0.73	0.70	0.75	0.75	0.67	0.90
40–43	0.74	0.72	0.76	0.76	0.69	0.91
43–46	0.75	0.73	0.78	0.78	0.71	0.91
46–50	0.77	0.75	0.79	0.79	0.72	0.92
50–55	0.79	0.77	0.81	0.81	0.74	0.93
55–60	0.81	0.79	0.83	0.82	0.77	0.94
60–70	0.82	0.81	0.85	0.84	0.79	0.95
70–100	0.87	0.85	0.89	0.88	0.84	0.98

Table 15: The dimuon acceptance \mathcal{A} calculated using the CMS measured polarization and its positive and negative uncertainties $\mathcal{A}(\sigma^\pm)$, and the values of the acceptance assuming no polarization $\mathcal{A}(\text{unpol})$, transverse polarization $\mathcal{A}(T)$, and longitudinal polarization $\mathcal{A}(L)$ for the $Y(3S)$ state and $0.6 < |y| < 1.2$.

p_T [GeV]	\mathcal{A}	$\mathcal{A}(\sigma^+)$	$\mathcal{A}(\sigma^-)$	$\mathcal{A}(\text{unpol})$	$\mathcal{A}(T)$	$\mathcal{A}(L)$
10–12	0.31	0.29	0.33	0.30	0.25	0.40
12–14	0.35	0.34	0.37	0.36	0.31	0.47
14–16	0.40	0.39	0.41	0.42	0.36	0.54
16–18	0.44	0.43	0.46	0.48	0.41	0.60
18–20	0.49	0.48	0.50	0.52	0.46	0.66
20–22	0.53	0.52	0.55	0.56	0.49	0.70
22–24	0.58	0.56	0.59	0.59	0.52	0.73
24–26	0.61	0.60	0.63	0.62	0.55	0.77
26–28	0.63	0.61	0.65	0.64	0.57	0.79
28–30	0.65	0.63	0.67	0.67	0.60	0.82
30–32	0.66	0.65	0.68	0.69	0.62	0.84
32–34	0.68	0.66	0.70	0.71	0.64	0.85
34–36	0.69	0.67	0.71	0.72	0.65	0.87
36–38	0.70	0.68	0.72	0.74	0.67	0.88
38–40	0.72	0.70	0.74	0.76	0.69	0.89
40–43	0.73	0.72	0.76	0.77	0.70	0.90
43–46	0.75	0.73	0.77	0.78	0.72	0.91
46–50	0.77	0.75	0.79	0.80	0.73	0.92
50–55	0.79	0.77	0.81	0.81	0.75	0.93
55–60	0.81	0.79	0.83	0.83	0.77	0.94
60–70	0.83	0.82	0.85	0.85	0.80	0.95
70–100	0.88	0.87	0.90	0.89	0.85	0.98

Table 16: The dimuon acceptance \mathcal{A} calculated using the CMS measured polarization and its positive and negative uncertainties $\mathcal{A}(\sigma^\pm)$, and the values of the acceptance assuming no polarization $\mathcal{A}(\text{unpol})$, transverse polarization $\mathcal{A}(T)$, and longitudinal polarization $\mathcal{A}(L)$ for the $Y(3S)$ state and $|y| < 1.2$.

p_T [GeV]	\mathcal{A}	$\mathcal{A}(\sigma^+)$	$\mathcal{A}(\sigma^-)$	$\mathcal{A}(\text{unpol})$	$\mathcal{A}(T)$	$\mathcal{A}(L)$
10–12	0.32	0.30	0.35	0.33	0.27	0.44
12–14	0.37	0.36	0.39	0.39	0.33	0.52
14–16	0.42	0.40	0.44	0.45	0.37	0.59
16–18	0.47	0.45	0.48	0.50	0.42	0.65
18–20	0.51	0.49	0.52	0.54	0.46	0.69
20–22	0.54	0.53	0.56	0.57	0.49	0.73
22–24	0.58	0.57	0.60	0.60	0.53	0.76
24–26	0.61	0.59	0.63	0.63	0.55	0.79
26–28	0.63	0.61	0.65	0.65	0.58	0.81
28–30	0.65	0.63	0.67	0.68	0.60	0.83
30–32	0.67	0.65	0.69	0.69	0.62	0.85
32–34	0.68	0.66	0.70	0.71	0.63	0.86
34–36	0.69	0.67	0.72	0.72	0.65	0.87
36–38	0.71	0.69	0.73	0.74	0.67	0.89
38–40	0.72	0.70	0.75	0.75	0.68	0.89
40–43	0.74	0.72	0.76	0.77	0.70	0.90
43–46	0.75	0.73	0.77	0.78	0.71	0.91
46–50	0.77	0.75	0.79	0.79	0.73	0.92
50–55	0.79	0.77	0.81	0.81	0.75	0.93
55–60	0.81	0.79	0.83	0.83	0.77	0.94
60–70	0.83	0.81	0.85	0.85	0.79	0.95
70–100	0.88	0.86	0.90	0.89	0.84	0.98

References

- [1] CMS Collaboration, “Measurement of the inclusive Υ production cross section in pp collisions at $\sqrt{s} = 7$ TeV”, *Phys. Rev. D* **83** (2011) 112004, doi:10.1103/PhysRevD.83.112004, arXiv:1012.5545.
- [2] CMS Collaboration, “Measurement of the $\Upsilon(1S)$, $\Upsilon(2S)$, and $\Upsilon(3S)$ cross sections in pp collisions at $\sqrt{s} = 7$ TeV”, *Phys. Lett. B* **727** (2013) 101, doi:10.1016/j.physletb.2013.10.033, arXiv:1303.5900.
- [3] ATLAS Collaboration, “Measurement of upsilon production in 7 TeV pp collisions at ATLAS”, *Phys. Rev. D* **87** (2013) 052004, doi:10.1103/PhysRevD.87.052004, arXiv:1211.7255.
- [4] LHCb Collaboration, “Measurement of Upsilon production in pp collisions at $\sqrt{s} = 7$ TeV”, *Eur. Phys. J. C* **72** (2012) 2025, doi:10.1140/epjc/s10052-012-2025-y, arXiv:1202.6579.
- [5] CMS Collaboration, “Measurement of the $\Upsilon(1S)$, $\Upsilon(2S)$ and $\Upsilon(3S)$ polarizations in pp collisions at $\sqrt{s} = 7$ TeV”, *Phys. Rev. Lett.* **110** (2013) 081802, doi:10.1103/PhysRevLett.110.081802, arXiv:1209.2922.
- [6] D0 Collaboration, “Measurement of inclusive differential cross sections for $\Upsilon(1S)$ production in $p\bar{p}$ collisions at $\sqrt{s} = 1.96$ TeV”, *Phys. Rev. Lett.* **94** (2005) 232001, doi:10.1103/PhysRevLett.94.232001, arXiv:hep-ex/0502030. [Erratum: doi:10.1103/PhysRevLett.100.049902].
- [7] CDF Collaboration, “ Υ production and polarization in $p\bar{p}$ collisions at $\sqrt{s} = 1.8$ TeV”, *Phys. Rev. Lett.* **88** (2002) 161802, doi:10.1103/PhysRevLett.88.161802.
- [8] P. L. Cho and A. K. Leibovich, “Color octet quarkonia production”, *Phys. Rev. D* **53** (1996) 150, doi:10.1103/PhysRevD.53.150, arXiv:hep-ph/9505329.
- [9] P. L. Cho and A. K. Leibovich, “Color octet quarkonia production. 2.”, *Phys. Rev. D* **53** (1996) 6203, doi:10.1103/PhysRevD.53.6203, arXiv:hep-ph/9511315.
- [10] K. Wang, Y.-Q. Ma, and K.-T. Chao, “ $\Upsilon(1S)$ prompt production at the Tevatron and LHC in nonrelativistic QCD”, *Phys. Rev. D* **85** (2012) 114003, doi:10.1103/PhysRevD.85.114003, arXiv:1202.6012.
- [11] G. Bodwin et al., “Quarkonium at the Frontiers of High Energy Physics: A Snowmass White Paper”, (2013). arXiv:1307.7425.
- [12] G. T. Bodwin, H. S. Chung, U.-R. Kim, and J. Lee, “Fragmentation contributions to J/ψ production at the Tevatron and the LHC”, *Phys. Rev. Lett.* **113** (2014) 022001, doi:10.1103/PhysRevLett.113.022001, arXiv:1403.3612.
- [13] B. Gong, L.-P. Wan, J.-X. Wang, and H.-F. Zhang, “Complete next-to-leading-order study on the yield and polarization of $\Upsilon(1S, 2S, 3S)$ at the Tevatron and LHC”, *Phys. Rev. Lett.* **112** (2014) 032001, doi:10.1103/PhysRevLett.112.032001, arXiv:1305.0748.
- [14] P. Artoisenet et al., “ Υ Production at Fermilab Tevatron and LHC Energies”, *Phys. Rev. Lett.* **101** (2008) 152001, doi:10.1103/PhysRevLett.101.152001, arXiv:0806.3282.

- [15] S. Baranov, “Prompt $Y(nS)$ production at the LHC in view of the k_t -factorization approach”, *Phys. Rev. D* **86** (2012) 054015, doi:10.1103/PhysRevD.86.054015.
- [16] P. Faccioli et al., “Quarkonium production in the LHC era: a polarized perspective”, *Phys. Lett. B* **736** (2014) 98, doi:10.1016/j.physletb.2014.07.006, arXiv:1403.3970.
- [17] CMS Collaboration, “Performance of CMS muon reconstruction in pp collision events at $\sqrt{s} = 7$ TeV”, *JINST* **7** (2012) P10002, doi:10.1088/1748-0221/7/10/P10002, arXiv:1206.4071.
- [18] CMS Collaboration, “The CMS experiment at the CERN LHC”, *JINST* **3** (2008) S08004, doi:10.1088/1748-0221/3/08/S08004.
- [19] D. Lange, “The EvtGen particle decay simulation package”, *Nucl. Instrum. Meth. A* **462** (2001) 152, doi:10.1016/S0168-9002(01)00089-4.
- [20] S. Agostinelli et al., “Geant4: a simulation toolkit”, *Nucl. Instr. Meth. A* **506** (2003) 250, doi:10.1016/S0168-9002(03)01368-8.
- [21] CMS Collaboration, “Measurements of inclusive W and Z cross sections in pp collisions at $\sqrt{s} = 7$ TeV”, *JHEP* **01** (2011) 080, doi:10.1007/JHEP01(2011)080, arXiv:1012.2466.
- [22] E. Barberio, B. van Eijk, and Z. W̑as, “PHOTOS: A universal Monte Carlo for QED radiative corrections in decays”, *Comput. Phys. Commun.* **66** (1991) 115, doi:10.1016/0010-4655(91)90012-A.
- [23] E. Barberio and Z. W̑as, “PHOTOS: A universal Monte Carlo for QED radiative corrections: Version 2.0”, *Comput. Phys. Commun.* **79** (1994) 291, doi:10.1016/0010-4655(94)90074-4.
- [24] W. Verkerke and D. P. Kirkby, “The RooFit toolkit for data modeling”, *eConf* **C0303241** (2003) MOLT007, arXiv:physics/0306116.
- [25] H. Akaike, “A new look at the statistical model identification”, *IEEE Transactions on Automatic Control* **19** (1974) 716, doi:10.1109/TAC.1974.1100705.
- [26] K. Burnham and D. Anderson, “Multimodel Inference: Understanding AIC and BIC in Model Selection”, *Sociological Methods Research* **33** (2004) 261, doi:10.1177/0049124104268644.
- [27] CMS Collaboration, “Absolute Calibration of the Luminosity Measurement at CMS: Winter 2012 Update”, CMS Physics Analysis Summary CMS-PAS-SMP-12-008, 2012.
- [28] G. Lafferty and T. Wyatt, “Where to stick your data points: The treatment of measurements within wide bins”, *Nucl. Instrum. Meth. A* **355** (1995) 541, doi:10.1016/0168-9002(94)01112-5.
- [29] J. Amundson, O. J. Eboli, E. Gregores, and F. Halzen, “Colorless states in perturbative QCD: Charmonium and rapidity gaps”, *Phys. Lett. B* **372** (1996) 127, doi:10.1016/0370-2693(96)00035-4, arXiv:hep-ph/9512248.
- [30] M. Butenschoen and B. A. Kniehl, “World data of J/ψ production consolidate NRQCD factorization at NLO”, *Phys. Rev. D* **84** (2011) 051501, doi:10.1103/PhysRevD.84.051501, arXiv:1105.0820.

- [31] M. Butenschoen and B. A. Kniehl, “Reconciling J/ψ production at HERA, RHIC, Tevatron, and LHC with NRQCD factorization at next-to-leading order”, *Phys. Rev. Lett.* **106** (2011) 022003, doi:10.1103/PhysRevLett.106.022003, arXiv:1009.5662.